Check for updates

Variation of structured laser beam pattern and optimization for an alignment reference line creation

WITOLD NIEWIEM,[1,2,*] KRYSTOF POLAK,[2,3] MARTIN DUSEK,[2,3] DIRK MERGELKUHL,[2] JEAN-CHRISTOPHE GAYDE,[2] ANDREAS WIESER,[1] AND MIROSLAV SULC[3,4]

[1]*ETH, Zurich, Switzerland*
[2]*CERN, Geneva, Switzerland*
[3]*TUL, Liberec, Czech Republic*
[4]*IPP CAS, Prague, Czech Republic*
[*]*witold.niewiem@cern.ch*

Abstract: The alignment of particle accelerators demands a dedicated measurement system based on a straight-line reference. This straight line can be provided by a laser beam. The alignment then involves accurately measuring the offset of accelerator components with respect to this light path. In order to be efficient, the laser beam needs to serve as a stable and straight reference for distances of several hundreds of meters. The attainable accuracy depends, among other parameters, on the laser spot size, which should ideally change very little over the distances at which the alignment system needs to operate. Due to the significant divergence of Gaussian laser beams, we propose using a structured laser beam (SLB) for alignment. Its transversal intensity profile is similar to a Bessel beam and consists of an intense inner core (IC) and concentric rings. The divergence of the IC, i.e., the growth of its size with distance, can be limited to 10 µrad using a favorable generator configuration. Thus an SLB may be suitable as a straight-line reference for long-distance alignment applications. However, the SLB is distorted if obstructions cover parts of the outermost ring (OR) of the beam within, which should therefore also be small. In this paper, we investigate the relationship between the size of the IC and OR depending on the design parameters of the SLB generator. We use numerical simulations and experiments with different generators over distances up to 50 m to analyze the transversal intensity profile and wavefronts of different SLBs. The results indicate the general suitability of an SLB as a reference line for long-distance alignment but also expose tradeoffs between small IC and small OR. The findings outlined in the paper help to describe the optimal SLB parameters for given conditions.

1. Introduction

Experimental setups, industrial production lines, and many other complex structures require individual elements to be arranged and kept in a specific geometric configuration with high accuracy. For elongated structures, this often involves arrangement with respect to a reference line, and the process of achieving this is called *alignment*. The key components of an alignment system are the reference line, the reference points on the elements to be aligned, and the measurement system used to quantify the offsets of the reference points from the reference line [1].

Particle accelerators are associated with particularly high demands regarding the alignment of elements along the desired particle beam path. Modern particle accelerators may require a relative alignment accuracy of 10 µm within a sliding window of 200 m length [2]. This means

that the reference points of the elements within this range must stay within a cylinder of 10 μm diameter, see Fig. 1.
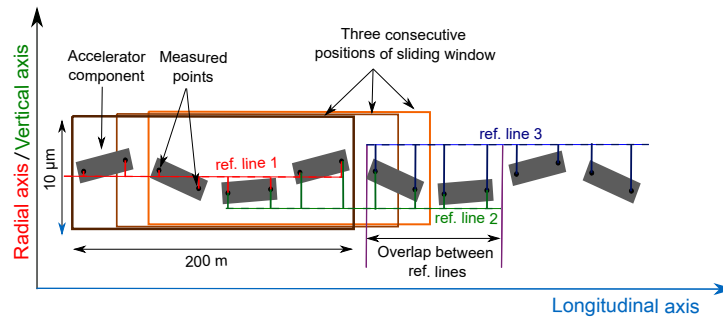

Fig. 1. Alignment offset measurement with respect to straight reference lines.

A reference line for alignment is either a physical object, such as a stretched wire, or an optical axis. In both cases, such a reference line can only be created over limited distances with desired accuracy. Large accelerators or accelerators with curved beam paths need multiple reference lines that overlap for the alignment. In such cases, technologies ensuring a straight and temporally stable reference line over long distances help to increase both accuracy and efficiency [3].

1.1. Gaussian beams and diffraction patterns

Reference lines based on Gaussian laser beams have been studied at CERN [3,4] and other institutes [5,6]. The use of such beams for alignment is problematic over large distances due to beam divergence. This is because it compromises detection at long distances due to the large size of the laser spot. The divergence decreases the measurement precision and necessitates larger and more expensive sensors. Various approaches have therefore been proposed to address these issues.

For Gaussian beams, the most common way to mitigate the negative influence of the beam divergence is to use beam expanders that adjust the position of the beam waist [7]. They allow the waist to be placed in the center of the measurement line thus improving the setup. However, the size of the laser spot at the beginning and the end of the line still complicates detection for long lines.

Another way to ensure a small laser spot is to focus the beam at a specific location. For long-distance alignment, this approach requires a focusing lens with a long focal distance, and lenses suitable for that purpose have a significant size. Fresnel plates have been proposed as an alternative [8–10]. A Fresnel plate focuses light exclusively on a single point, thus only allowing the measurement of an offset at this particular point, with the laser spot significantly larger in other places. The laser source, the Fresnel plate, and the sensor establish a three-point alignment system, where the offset of the middle point equipped with the Fresnel plate is measured with respect to the line defined by the source and the detector. To measure the offset of another point, a different Fresnel plate has to be used with different focusing characteristics. In addition, any displacement of elements along the reference line results in a blurred spot at the new location, so decreasing the measurement accuracy.

An alternative approach to overcome the beam divergence is to use a so-called Poisson pattern [11]. Such a pattern is created by non-transparent ball targets attached to the accelerator elements. A Gaussian beam is projected onto the ball targets and each one casts a shadow at the end of the measurement line, where the detector is placed. The light diffracted on the edges of the balls creates a small diffraction dot in the middle of the shadow. The detector at the end of the line measures the offsets between diffraction dots, and thus the offsets of the accelerator elements.

This method allows multiple points to be measured at the same time, but their number is limited by the transversal width of the Gaussian beam spot. Furthermore, the diffraction patterns created by multiple balls overlap, making the detection challenging. Research on a Poisson alignment system was reported by [12,13], with such a system operationally used for accelerator positioning at DESY [14].

Airy diffraction patterns, from a light beam that passes through a circular aperture, can also be used for accelerator alignment with the advantage that it can be preserved over long distances. This approach has been used at SPring-8 [15] and KEK [16]. While such a system can reduce beam divergence down to 250 µrad, precise generator alignment and nearly perfect iris geometry are required to produce a symmetrical pattern.

1.2. Bessel beams

Non-diffractive beams are optical beams with theoretically zero divergence. An example of this class are the so-called Bessel beams. Their transversal profile is described by the Bessel function of a given order [17]. There are multiple ways to generate such beams, such as using an axicon [18], a volume holographic method [19], or meta-surfaces [20]. Bessel beams find many applications in science and industry [21] thanks to their propagating invariance (constant shape and size along the direction of propagation) and self-healing ability (the regeneration of the pattern after an obstacle that partially obscures the transversal profile of the beam) [22].

Even though generated Bessel beams are not perfectly non-diffractive, they still have significantly lower divergence than conventional Gaussian beams. Bessel beams have been proposed for the alignment of optical elements at short distances due to the compactness of the inner core [23]. Nevertheless, due to the finite aperture of the generator, they can propagate only over a limited distance. That distance depends on the technology used but has so far only been theoretically demonstrated up to 140 m [24].

1.3. Structured laser beams

A Structured Laser Beam (SLB) is the proper name for a novel type of optical beam introduced in the patent [25] and described in further detail in [26–28]. SLBs share similarities with Bessel beams and Laguerre-Gaussian (LG) beams. The similarities are visible for an LG beam with zero azimuthal mode and higher radial modes. All these beams fall under the broad category of structured light, known for their structured distributions of intensity, polarization, or phase, as discussed in references [29–31]. Currently, the analytical description for an SLB is not available; thus, we conducted tests to harness their potential for alignment purposes.

An SLB exhibits some characteristics of non-diffractive beams and shares a transverse intensity profile akin to that of a Bessel beam. It consists of a narrow inner core (IC) and surrounding concentric rings, amongst which the biggest one is the outer ring (OR), see Fig. 2. An SLB is suitable for long-distance alignment due to the low divergence of the IC, with a divergence of 10 µrad having been achieved [27]. An SLB can theoretically propagate to infinity and has been experimentally tested up to 900 m with a setup similar to the one described in [27]. The transversal intensity of the SLB at this distance in this experiment is presented in Fig. 3.

In this paper, we derive a method for determining the IC and OR size depending on the generator setup and the distance from the generator. These relationships have not been discussed previously and are crucial for the practical use of an SLB for alignment. The divergence of the IC and the OR is characterized through both simulations and experiments. The IC size is important as it determines the sensor dimensions of the alignment system, while the OR diameter is important due to its impact on the symmetry breaking of an SLB. The latter causes the light path of the SLB to change when it passes through an aperture partially covering the transversal profile area encircled by the OR [28]. The magnitude of this change may be detrimental to alignment applications. Such a change does not occur if the transversal profile of the SLB is

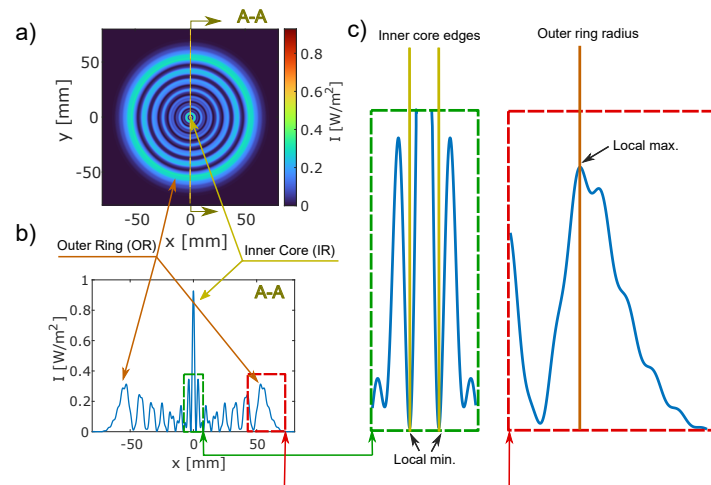**Fig. 2.** a) The simulated transversal intensity distribution of an SLB at 225 m from the generator, b) a profile through the center of the transversal intensity distribution, and c) the definition of the inner core (IC) and outer ring (OR) edges.
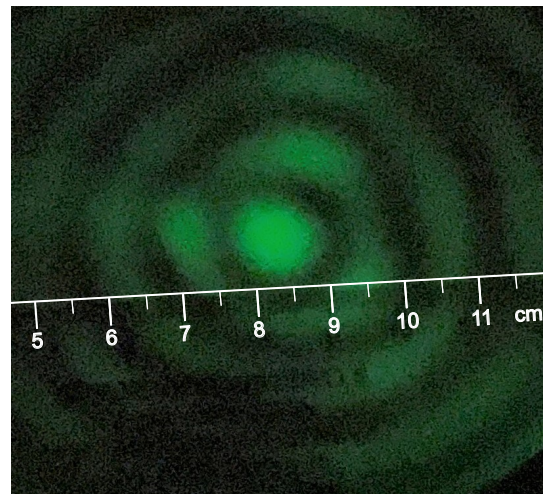

Fig. 3. Image of the transversal intensity distribution of an SLB at 900 m from the generator, with an indicative scale bar (outer ring outside image).

unimpeded within the OR. A small OR diameter is thus favorable for alignment, as it puts fewer constraints on any obstacles that may interfere with the SLB.

2. Methods

2.1. Principle of generation

The shape of the wavefront of an SLB varies with the propagation distance. In this study, we focus on the wavefront directly after the generator, which can be described analytically. The SLB wavefront h_s is a combination of two rotationally symmetric optical effects with opposite signs: a spherical aberration and a defocus. We denote the rotation axis as the z-axis. The combination is expressed in Eq. (1), where z is the position along the z-axis of a point P that is part of h_s, ρ is the relative radius of the P position from the z-axis in the transversal direction, K_D is the defocus coefficient, and K_{Sn} are the spherical aberration coefficients.

$$h_s : z = K_D\rho^2 + \sum_{n=1}^{\infty} K_{Sn}\rho^{2(n+1)} \tag{1}$$

The relative radius is the ratio of r and the maximal possible radial position r_{max} of P (Eq. 2), where r_{max} is limited by the output aperture of the generator.

$$\rho = \frac{r}{r_{max}} \tag{2}$$

Fig. 4 shows a cross-section of the wavefront in the xz-plane of a cartesian coordinate system with x- and y-axes perpendicular to the z-axis; r is indicated for a point P in this cross-section. The output vertex of the SLB generator is at the distance $z = 0$.
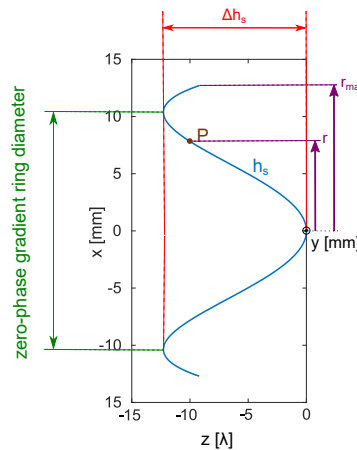
Fig. 4. The wavefront profile of an SLB directly after the generator with wavefront (h_s), radius (r) of the point (P), maximal possible radial position (r_{max}), depth of wavefront (Δh_s).

The simulations presented in the paper use two procedures. A ray tracing approximation is used to track light through the generator to give the phase and amplitude distribution directly after the optical system. Propagation in free space after the generator assumes the wave nature of the light and linearity of the system with the phase and amplitude obtained after the generator as input. A transfer function is thus used for short-distance simulations and the Fresnel approximation of the diffraction integral for distances exceeding 10 m [32].

The SLB generator, creating spherical aberration and defocus, acts like a Keplerian beam expander conserving the almost parallel character of input and output beams while inducing a phase delay. The phase delay contributes to the specific wavefront shape with a zero-phase gradient ring, where the gradient is considered along the radial direction. The diameter of the zero-phase gradient ring and the distance variation Δh_s of the wavefront within this ring, see Fig. 4, serve as important parameters to characterize the long-distance propagation of an SLB.

An SLB can be generated using multiple generation principles [25]. The generator used for the investigations cited in this paper consists of a laser source, a ball lens, and a plano-convex projection lens. See Fig. 5. Any modification of these elements or their position affects the SLB wavefront and the intensity distribution. The ball lens plays a key role in the optimization of energy efficiency. The diameter $\varnothing_S$ of the coherent light beam (wavelength λ_S) entering the generator and the diameter $\varnothing_{BL}$ of the ball lens affect the intensity of an SLB. The ball lenses were illuminated with $\varnothing_S > \varnothing_{BL}$ during the experiments presented in this paper since energy efficiency was not the main focus of the present research.

Fig. 5. The schematic of the SLB generator with laser source (S), ball lens (BL), projection lens (PL), laser source wavelength (λ_S), diameters ($\varnothing_S$, $\varnothing_{BL}$, $\varnothing_{PL}$), refractive indices (n_{BL}, n_{PL}), radii of lenses (R_{BL}, R_{PL}), distances (L_{PL}, L_{PLmax}, L_{PLmin}), projection lens thickness (T_{PL}), see Sec. 2.4 for values of the parameters.

2.2. Focusing of generator

The distance L_{PL} between the ball lens and the projection lens is important for the transversal intensity profile of the SLB as it defines focusing of the generator. We propose the definition of a parameter ξ to enable the comparison of these distances across various generators. This parameter indicates the relative location of the chosen value of L_{PL} between two values L_{PLmin} and L_{PLmax}, see Eq. (3). L_{PLmin} is the value of L_{PL} for which the radius of the zero-phase gradient ring is equal to r_{max}, while L_{PLmax} is the value of L_{PL} for which Δh_s is zero. They represent the minimum and maximum of L_{PL} for which the generator produces an SLB with an infinite range.

$$L_{PL} = L_{PLmin} + \xi(L_{PLmax} - L_{PLmin}) \tag{3}$$

For the analyses carried out later we determined these values numerically by iteratively adjusting the L_{PL} used for the simulation of the SLB wavefront and intensity. When the focal points of both optical elements are at the same location, $K_D = 0$ and $L_{PL} = L_{PLmax}$. This occurs when the generator is illuminated by a plane wave with the wave vector parallel to the z-axis, Fig. 6.

L_{PLmax} can then be found analytically through Eq. (4), Eq. (5) and Eq. (6).

$$L_{PLmax} = f_{BL} - U_{BL} + f_{PL} - U_{PL} \tag{4}$$

$$f_{BL} = \frac{n_{BL0} R_{BL}}{2(n_{BL0} - 1)} \qquad f_{PL} = \frac{R_{PL}}{n_{PL0} - 1} \tag{5}$$

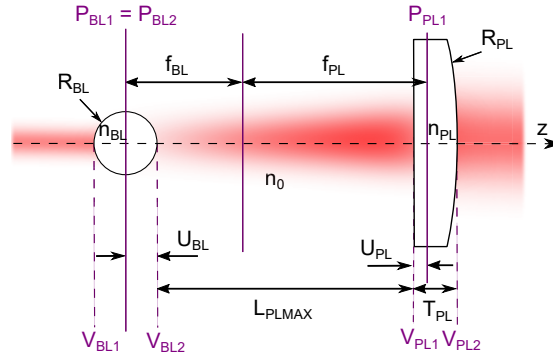$$U_{BL} = R_{BL} \qquad U_{PL} = \frac{T_{PL}}{n_{PL0}} \tag{6}$$

Fig. 6. Generator setup with ball lens (*BL*), projection lens (*PL*), the paraxial focal lengths (f_{BL}, f_{PL}), distances (U_{BL}, U_{PL}) between the principal points (P_{BL2}, P_{PL1}) and the surface vertices (V_{BL2}, V_{PL1}), refractive indices (n_{BL}, n_{PL}, n_0), radii of lenses (R_{BL}, R_{PL}), projection lens thickness (T_{PL}), see Sec. 2.4 for values of the parameters. $L_{PL} = L_{PLmax}$ for illumination by plane waves along the *z*-direction.

Here f_{BL} is the paraxial focal length of the ball lens and f_{PL} is the focal length of the projection lens. n_{BL0} and n_{PL0} are the refractive index ratios of the ball lens and projection lens refractive indices, n_{BL} and n_{PL}, with that of the refractive index of the surroundings n_0. R_{BL} R_{PL} are the radii of the ball lens and the projection lens respectively. U_{BL} is the distance between the principal point and the surface vertex of the ball lens and U_{PL} is the distance between the principal point and the surface vertex of the projection lens. T_{PL} is the thickness of the projection lens.

For $\xi \in (0, 1)$, the IC and the OR appear immediately after the generator and remain visible at any distance provided the source laser has enough power. The shapes of the wavefronts for a specific laser source, ball lens, and projection lens as a function of different values of ξ are shown in Fig. 7, along with the zero-gradient rings (green dots) in transverse cross-section. For $\xi > 1$, an SLB is only created in a limited range, with the IC and the OR disappearing after a certain distance, similar to Bessel beams. For $\xi < 0$, no SLB is created, as no IC is formed.

2.3. IC and OR description

Currently, there is no closed-form formula available to calculate the diameter of the IC and OR at different distances from the generator using design parameters such as λ_S, $\varnothing_S$, $\varnothing_{BL}$, L_{PL}, etc. Numerical simulations are therefore employed to calculate the intensity distribution of the SLB in the transversal plane for specific design parameters and distances. The IC and OR are then determined by analyzing the transverse intensity profiles.

In the laboratory, this transversal intensity profile of the SLB is measured using a camera, which is then compared to the simulated results. To identify the edge of the IC in both the measured and simulated data, we use the resemblance between an SLB and a Bessel beam in the central region of these beams. The IC edge is defined as the closest local minimum encircling the center of the IC in the fitted Bessel beam, as shown in Fig. 2.
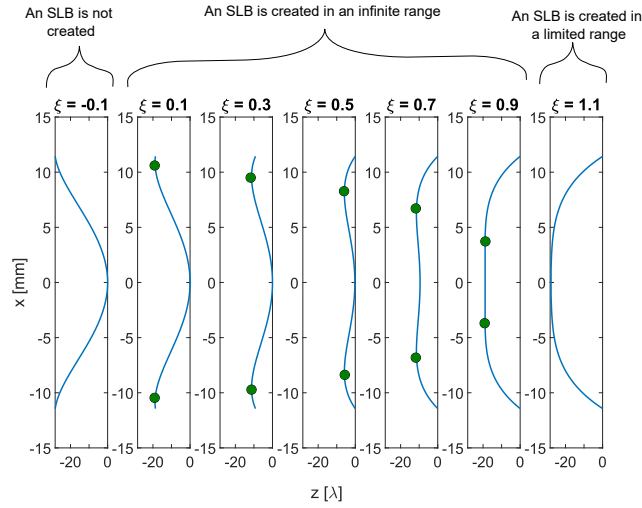
Fig. 7. Changes of the wavefront shape directly after the projection lens depending on the ξ parameter for a generator with the following properties: $\varnothing_{BL}$ = 4.0 mm, R_{PL} = 38.6 mm, T_{PL} = 4.1 mm, $n_{BL} = n_{PL}$ = 1.5199, n_0 = 1.0003). In this case L_{LPmax} = 70.54 mm and L_{LPmin} = 72.53 mm.

The OR is defined as the outermost intense ring beyond which the intensity decreases to values close to zero. In the laboratory, the radius of the OR is measured using a ruler. This method captures the most intense part of the OR. For the simulated data, we adjust the OR measurement to align with that found in the laboratory. The radius of the OR is determined by analyzing the transverse intensity profile in an arbitrarily chosen direction and identifying the radial position of the peak intensity (local maximum) within the outer ring, as illustrated in Fig. 2.

An approximate method to calculate the IC diameter is proposed, this being important for the design of an alignment system. This approach is based on the analogy between the central parts of an SLB and a Bessel beam, as depicted in Fig. 8. The intensity distribution of a Bessel beam is described by Eqs. (7) and (8).

$$I = I_0(J_0(k_T r))^2 \tag{7}$$

$$k_T = \frac{2\pi}{\lambda_S} \sin(\theta) \tag{8}$$

Here, I_0 is a constant intensity, J_0 is the zero-order Bessel function of the first kind, and θ represents the angle between the wave vector k and its longitudinal component k_L. Transversal component is k_T.

For the Bessel beam, the IC edge corresponds to the local minimum closest to the center of the IC. This edge occurs at a radial distance r_0, where the argument of the Bessel function is equal to the first root γ of the Bessel function ($\gamma \approx 2.4048$), thus satisfying $k_T r_0 = \gamma$.

In the case of an SLB, the IC is created in a similar manner to that of the Bessel beam, with the assumption of neglecting the contribution from the central part of the wavefront, which is not present in the Bessel beam. However, in reality, the central part contributes to the transversal intensity profile, leading to subtle changes in the IC size. These changes are evident in the results shown in Fig. 10. When an SLB is generated, the value of θ varies, as illustrated in Fig. 8, resulting in different IC sizes depending on the longitudinal position L of the transversal profile. The approximate IC diameter of an SLB can be calculated using Eq. (9), where $1/\sin(\theta)$ can be replaced by the square root expression with the assumption of neglecting the thickness of the

wavefront.

$$IC \approx \frac{\gamma \lambda_S}{\pi \sin(\theta)} \approx \frac{\gamma \lambda_S}{\pi} \sqrt{1 + \frac{L^2}{r^2}} \tag{9}$$
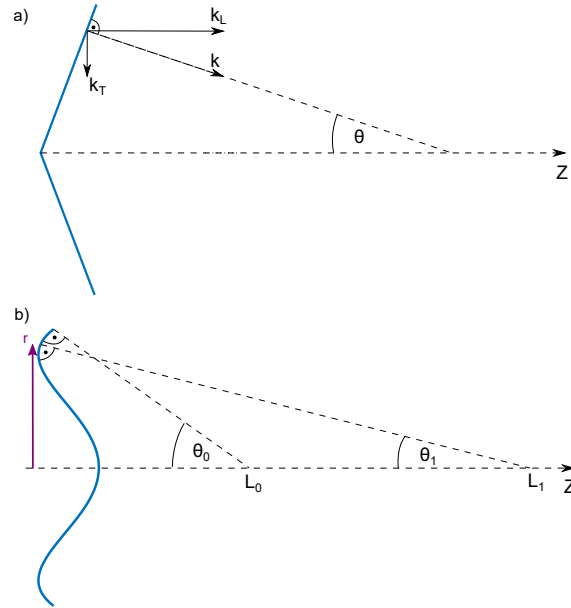

Fig. 8. Schematic profiles of a Bessel beam a) and an SLB b) wavefront with wave vector (k), longitudinal component (k_L), transversal component (k_T), angle (θ) between (k) and (k_L), radius (r), longitudinal position (L).

2.4. Experimental setups

Two experimental setups were constructed to verify the simulation results and examine the properties of the generated SLBs. The first setup was a laboratory arrangement of different generators, a Shack-Hartman sensor for measuring the wavefronts and a Basler camera a2A5328-15umPRO for the transversal intensity profile at a distance of 10 m from the generator. This setup used a laser diode, CPS635 from Thorlabs ($\lambda_S = 635$ nm), a ball lens of sapphire ($\varnothing_{BL} = 5$ mm, $n_{BL} = 1.7658$), and two different plano-convex projection lenses with a diameter of $\varnothing_{PL} = 9$ mm made of BK7 glass ($n_{PL} = 1.5150$): a lens F12 ($R_{PL} = 6.2$ mm, $T_{PL} = 3.4$ mm), and a lens F20 ($R_{PL} = 10.3$ mm, $T_{PL} = 2.5$ mm). The Shack-Hartman sensor consisted of a microlens array MLA300-14AR from Thorlabs combined with a Basler camera a2A5328-15umPRO. The Shack-Hartman sensor was calibrated with a planar wavefront source. The wavefront shape was calculated using in-house software [33]. This experiment was aimed at comparing the impact of various generator configurations on the wavefront shape and intensity distribution.

The second setup for the IC and OR size investigation was installed in a 50 m-long underground tunnel. The SLB generator was mounted at a fixed position on a rail running along the length of the tunnel. The Basler camera, serving as a detector, was moved along the rail in steps of approximately 2 m from a distance of 2 to 50 m from the generator. A photo was acquired after each step, resulting in a total of 25 images of the transversal beam profile at different distances. For this experiment, three SLB generators were used based on a CPS532 laser diode from Thorlabs ($\lambda_S = 532$ nm), a ball lens of BK7 glass ($\varnothing_{BL} = 4.0$ mm, $n_{BL} = 1.5195$) and three different plano-convex projection lenses with $\varnothing_{PL} = 25.4$ mm, made of BK7 glass ($n_{PL} = 1.5195$): F50

($R = 13.1$ mm, $T_{PL} = 5.3$ mm), F75 ($R = 38.6$ mm, $T_{PL} = 4.1$ mm), and F100 ($R = 51.5$ mm, $T_{PL} = 3.9$ mm). Data were then acquired using generator settings with L_{PL} set for ξ-values of 0.2, 0.4, 0.6, 0.8, based on the L_{PLmin} and L_{PLmax} determined by simulation (see Sec. 2.1).

ξ was set to its target values by modifying L_{PL}, the distance between the ball lens and the projection lens. The projection lens remained in the same position while the ball lens was displaced using an SM1NR1-SM1 zoom housing from Thorlabs. This is a one-dimensional translation stage that allows L_{PL} to be changed while maintaining the overall generator alignment. The initial distance was set to L_{PLmin}, i.e. $\xi = 0$, which was simulated for each generator. L_{PLmin} was measured using a Leica AT401 laser tracker. The surfaces of the ball lens and the projection lens were measured using a 0.5-inch Leica Red-Ring Reflector (RRR). The ball lens and projection lens surfaces were calculated by fitting appropriate geometrical primitives (sphere, plane) to the measured points. The manual movement of the ball lens using the zoom housing was conducted based on a visual reading of the engraved scale on the housing, where each tick indicated 0.25 mm of translation. The precision of ball lens positioning is 0.10 mm including the laser tracker measurement, the precision of readings and the mechanical repeatability of the zoom housing.

3.   Results and discussion

3.1.   *Wavefront and intensity distribution*

Figure 9 illustrates representative measurements of the intensity distribution in the transversal plane along with their cross-sections and wavefronts for different projection lenses (see Sec. 2.4) and L_{PL} distances.
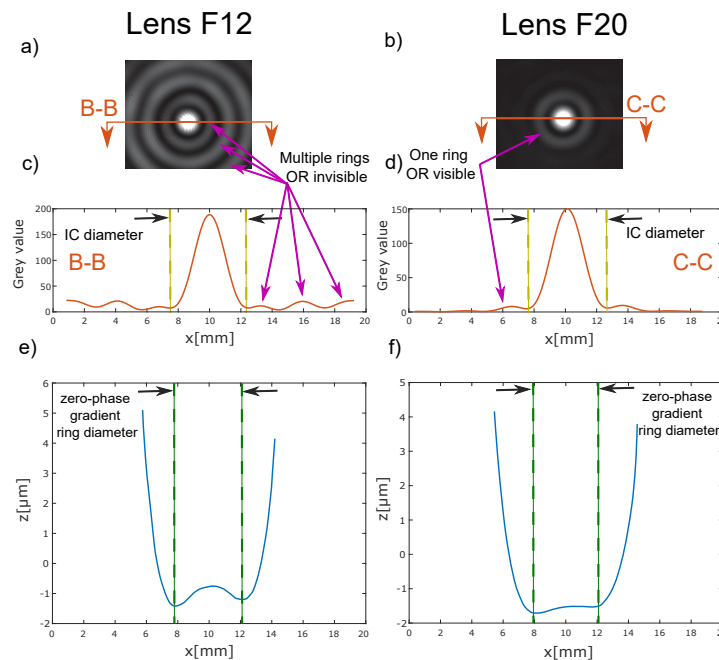

Fig. 9. Intensity distributions in the transversal plane at 10 m from the generator (a), (b), intensity distribution profiles through the IC center (c), (d), and wavefront profiles acquired immediately following the generator (e), (f) for two laboratory setups with different projection lenses and ξ values.

The two setups were manually adjusted by changing L_{PL} such that the measured zero-phase gradient ring diameter of the second setup was within 5% of the first setup. Consequently, the L_{PL} and ξ were different for these two setups. However, it can be observed from Fig. 9 (c and d) that the width of the IC is similar for both SLBs. Conversely, the number of rings and the diameters of the respective ORs differ. The projection lens with a longer focal length (F20) results in a smaller diameter OR, which is preferable to avoid excessive symmetry breaking of an SLB in long-distance applications.

It is important to note that the diameter of the IC is not equal to the diameter of the zero-phase gradient ring. However, within our experiments, we consistently found that two SLBs with equal zero-phase gradient ring diameters also have equal IC diameters. Additionally, a larger zero-phase gradient ring is associated with a smaller IC diameter. Considering that a smaller IC is generally preferable for high-precision alignment, generators with a large zero-phase gradient ring are therefore desirable. In practice, the size of this ring is limited by the aperture $\varnothing_{PL}$ of the projection lens, with a large aperture required for a small IC. The large zero-phase gradient ring ensures a favorable value of θ in the approximate Eq. (9), thereby reducing the IC size. However, the impact of increasing aperture size is limited by the divergence of the beam coming from the ball lens [25] as the projection lens needs to be entirely illuminated to fully benefit from its aperture.

3.2. Long-distance propagation

The second experimental setup described in Sec. 2.4 was employed to investigate the transverse profile of the SLB over propagation distances of up to 50 m. The aim was to examine the influence of different generators, each adjusted to a common value of $\xi = 0.4$. Fig. 10 and Fig. 11 illustrate the simulated, measured, and analytically determined diameters of the IC and OR as a function of the distance from the generator. It can be seen that the simulation results exhibit a good agreement with both the measurements and analytical derivation.

The IC is not formed below a certain distance from the projection lens due to the underlying creation mechanism of the SLB. Determining the exact IC creation distance is challenging because of the similarity of the diffraction pattern also created at the beginning of an SLB path, which might explain the irregular behavior of the simulated IC size observed at the initial stages of propagation in Fig. 10. Defining the position of this boundary between the diffraction pattern and the IC of an SLB is important for future alignment applications as it will determine the location of the nearest element that can be measured.

In the far optical zone (Fraunhofer zone), the divergence of the IC and OR follows a linear relationship, with the size of the IC and OR increasing proportionally to the distance from the generator. However, in the near optical zone (Fresnel zone) deviations from this linearity can be observed. These deviations are more pronounced for the OR, particularly when using longer focal lengths for the projection lenses, as seen in Fig. 11. The exact position of the boundary between the near and far optical zones depends on the specific characteristics of the generator. In addition, the SLB pattern observed in the near optical zone undergoes significant changes, including alterations in the number of rings, their intensity, and their spacing. As the distance increases the pattern stabilizes, with the size becoming directly proportional to the distance. In the context of long-distance alignment scenarios, the application of an SLB will predominantly occur in the far optical zone, allowing us to approximate the IC divergence through a linear relationship with distance from the generator.

Figure 12 illustrates the distinct relationships between the IC and OR diameters for a generator equipped with an F50 projection lens at various distances and for various values of ξ. The blue lines show the results obtained from numerical simulations for propagation distances of 30 m, 40 m, and 50 m. While the points along each line correspond to different values of ξ, ranging from
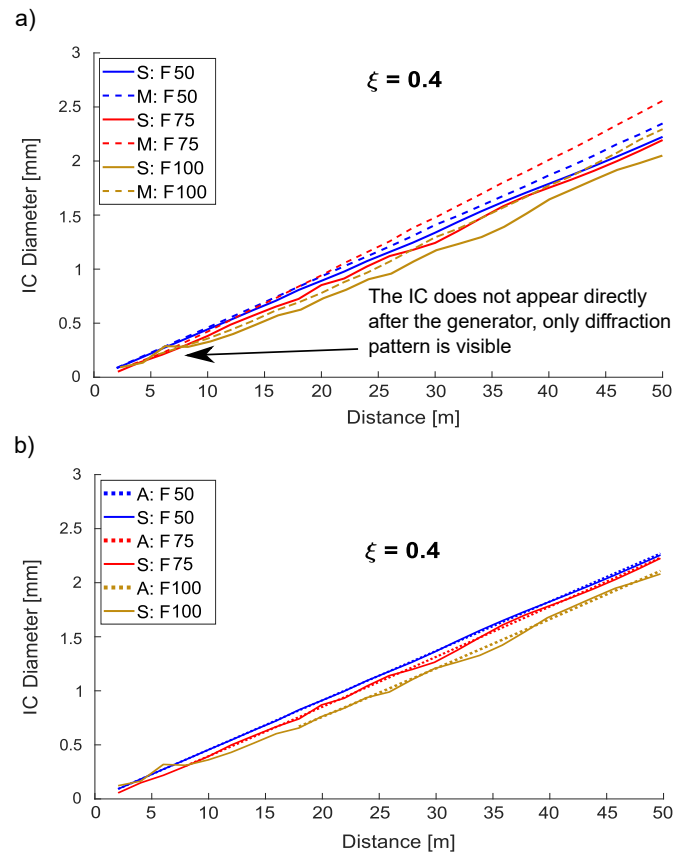
a)

b)

Fig. 10. The diameter of the IC as a function of the distance from the generator: a) results based on simulation (S) and measurement (M) with different setups see Sec. 2.4; b) results based on numerical simulation (S) see Sec. 2.1 and the analytical function (A) see Sec. 2.3.

$\xi = 0$ (bottom right) to $\xi = 1$ (top left). The colored dots represent specific IC-OR combinations corresponding to measurements and simulations at ξ values of 0.2, 0.4, 0.6, and 0.8.

From Fig. 12, we observe that smaller IC diameters correspond to larger OR diameters and vice versa, irrespective of the distance. This relationship highlights the tradeoff that has to be made between the required detector size and the available propagation space within the alignment system.

The measured data points all lie on the lines derived from numerical simulations but appear to be shifted in the same direction along the lines compared to the simulation result for the corresponding ξ value. These discrepancies can be attributed to a systematic difference in the setting of L_{PL} by the zoom housing. Data analysis suggests that this systematic difference between L_{PL} values derived from simulations and measurements has a size of 0.38 mm on average, with a standard deviation of 0.10 mm. Despite the L_{PL} discrepancies, the simulated values provide a reliable approximation of the IC and OR sizes. Through simulation, it is possible to determine generator parameters that enable the attainment of desired IC and OR sizes, meeting the requirements of the alignment system's reference line.
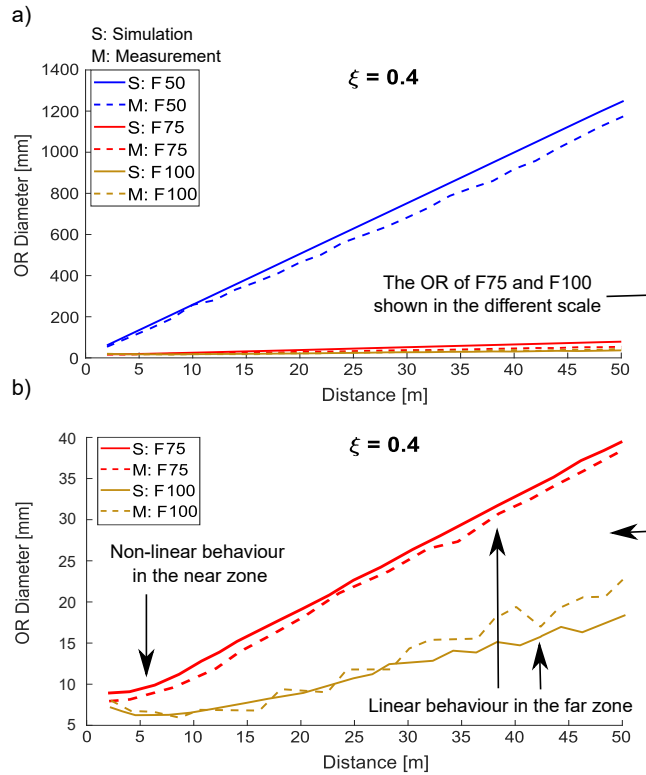
Fig. 11. a) The diameter of the OR as a function of the distance from the generator; b) the same but plotted with a different scale; results based on simulation (S) and measurement (M) with different setups see Sec. 2.4.
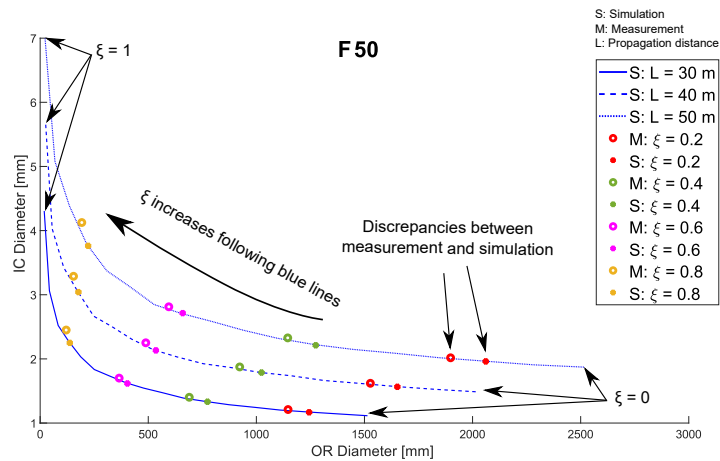

Fig. 12. Simulation (S) of the IC and OR size compared to measured (M) values for different distances and generator configurations.

3.3. Impact of generator focusing on IC and OR

The simulated data presented in Fig. 13 summarize the dependence of IC and OR on ξ. The data consider a fixed distance of 50 m using the second experimental setup introduced in Sec. 2.4. It shows the influence on these quantities of the generator design, namely the choice of L_{PL} distance for a given ball lens, projection lens, and source illumination.
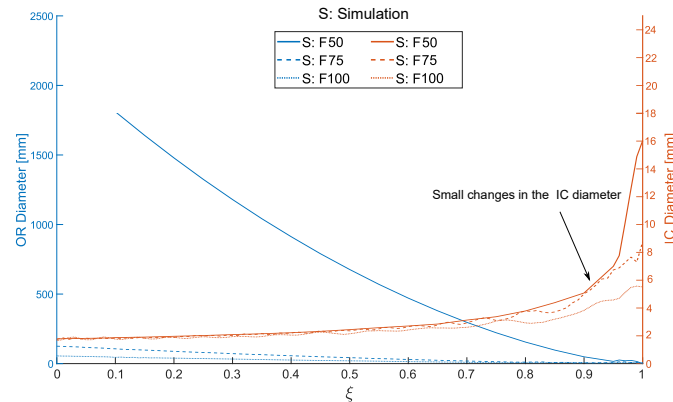

Fig. 13. Simulation of the IC (orange) and OR (blue) size at 50 m as a function of ξ for different projection lenses (F50, F75, F100).

Small differences in the IC size from the trend can be observed when changing the ξ parameter for the setups with F75 and F100 projection lenses. These size variations are related to the intensity changes in the IC. The IC and its close vicinity are primarily influenced by interfering contributions from two different parts of the SLB wavefront. The first area corresponds to the central part around the z-axis, and the second area is the region of the zero-phase gradient ring, as shown in Fig. 4. The phase difference between these areas contributes to the IC intensity variation. When the ξ parameter is changed, the phase difference takes values of $0, 2\pi, 4\pi, \dots$ rad, resulting in constructive interference between the contributions from both areas. Conversely, for other values of ξ, these contributions interfere destructively at $\pi, 3\pi, 5\pi, \dots$ rad phase differences. This constructive and destructive interference affects the position of the first local minimum in the intensity distribution in the transversal plane, thus limiting the IC size. Consequently, the size of the IC changes with the ξ parameter.

4. Conclusion

The study of an SLB for application to a straight reference line for alignment purposes has provided comprehensive insights into the divergence of the IC and OR, and the dependence of their transversal size on the generator parameters and propagation distance. The correlation between the size of the IC and OR implies that a suitable tradeoff has to be found for future alignment purposes, to balance the detector size with the available propagation space.

In this paper, we have characterized the SLB generation principle and the basic parameters of a generator composed of a ball lens and a projection lens. Through our investigations, we have confirmed that a longer focal length of the projection lens results in a smaller OR, thereby optimizing the generator for its desired performance for long-distance alignment purposes. In order to facilitate the comparison between different generators, we have introduced a new parameter, denoted as ξ, which serves as a common descriptor of generator focusing. The value of ξ is derived from the distance between the ball and projection lenses, with its minimization leading to reduced IC divergence.

Additionally, we have described the SLB wavefront by introducing the zero-phase gradient ring parameter. By increasing the aperture of the projection lens, we can achieve a larger zero-phase gradient ring diameter, which subsequently results in a smaller IC. It is important to note that the divergence of the IC and OR is non-linear in the near, Fresnel zone. For long-distance alignment applications, the propagation will occur predominantly in the far, Fraunhofer zone, where the SLB divergence is approximately linear with distance.

Future investigations should prioritize the examination of SLB intensity, the characterization of which will further enhance the understanding of SLBs and their application to future alignment systems.

Disclosures. The authors declare no conflicts of interest.

Data availability. Data underlying the results presented in this paper are not publicly available at this time but may be obtained from the corresponding author upon reasonable request.

References

1. R. E. Ruland, "Alignment considerations for the next linear collider," in *Particle Accelerator Conference*, vol. 3 (IEEE, 1995), pp. 2009–2013.
2. R. J. Leao, C. R. Baldo, M. L. C. D. C. Reis, and J. L. A. Trabanco, "Engineering survey planning for the alignment of a particle accelerator: Part I. proposition of an assessment method," Meas. Sci. Technol. **29**(3), 034006 (2018).
3. G. Stern, "Study and development of a laser based alignment system for the compact linear collider," Ph.D. thesis, ETH Zurich (2016).
4. J.-P. Quesnel, "Development of an accurate laser alignment, operated in a vacuum pipe," *International Congress, Melbourne, Australia* (1994).
5. A. Reichold, M. Dawson, J. Green, Y. Han, M. Jones, G. Moss, B. Ottewell, D. Kämtner, J. Prenting, M. Schlösser, and G. Grzelak, "The LiCAS-RTRS-A rapid and cost efficient survey system for the ILC," in *9th International Workshop on Accelerator Alignment*, September 26-29 (2006).
6. V. Batusov, J. Budagov, M. Lyablin, J. C. Gayde, B. D. Girolamo, D. Mergelkuhl, and M. Nessi, "The laser fiducial line measurement precision in open air media determined in comparison with laser tracker AT-401," Phys. Part. Nuclei Lett. **12**(2), 297–304 (2015).
7. D. P. G. Stern, A. G. J. Sandomierski, M. Sosin, S. Guillaume, and H. Mainaud-Durand, "Experiment of laser pointing stability on different surfaces to validate micrometric positioning sensor," in *International Particle Accelerator Conference (7th)* (2016).
8. N. Deelen, "Pre-alignment of clic RASCLIC versus WPS," Master's thesis, Utrecht University (2015).
9. T. Luo, Z. Q. He, H. Cheng, T. S. Zuo, S. W. Xiao, S. Lu, Z. Y. Ke, N. Ma, T. Wang, J. Liang, L. Dong, X. L. Wang, B. Li, and L. L. Men, "A new laser-based alignment method for the multi-slits VSANS in high precision," Nucl. Instrum. Methods Phys. Res., Sect. A **1010**, 165526 (2021).
10. T. Suwada, M. Satoh, S. Telada, and K. Minoshima, "Experimental investigation on focusing characteristics of a He-Ne laser using circular fresnel zone plate for high-precision alignment of linear accelerators," Rev. Sci. Instrum. **83**(5), 053301 (2012).
11. J. E. Harvey and J. L. Forgham, "The spot of arago: New relevance for an old phenomenon," Am. J. Phys. **52**(3), 243–247 (1984).
12. L. V. Griffith, R. F. Schenz, and G. E. Sommargren, "Magnetic alignment and the poisson alignment reference system," Rev. Sci. Instrum. **61**(8), 2138–2154 (1990).
13. I. Feier, H. Friedsam, and M. Penicka, "The poisson alignment reference system implementation at the advanced photon source," in *5th International Workshop on Accelerator Alignment* (1999).
14. C. Schwalm, "Straight line reference system. status report on poisson system calibration straight line reference system," in *IWAA 2012 Fermilab* (2012).
15. C. Zhang, M. Hasegawa, K. Kanda, and T. Shinomoto, "Performance of the iris diaphragm laser alignment system of the SPring-8," in *13th International Workshop on Accelerator Alignment* (2014).
16. M. Satoh and T. Suwada, "Design of collimated laser beam optics for the KEKb injector linac alignment system," in *Linear Accelerator Conference* (2010).
17. J. Durnin, "Exact solutions for nondiffracting beams. i. the scalar theory," J. Opt. Soc. Am. **4**(4), 651–654 (1987).
18. J. H. McLeod, "The axicon: A new type of optical element," J. Opt. Soc. Am. **44**(8), 592–597 (1954).
19. A. J. Asuncion and R. A. Guerrero, "Generating superimposed bessel beams with a volume holographic axicon," Appl. Opt. **56**(14), 4206 (2017).
20. W. T. Chen, M. Khorasaninejad, A. Y. Zhu, J. Oh, R. C. Devlin, A. Zaidi, and F. Capasso, "Generation of wavelength-independent subwavelength bessel beams using metasurfaces," Light: Sci. Appl. **6**(5), e16259 (2016).
21. S. N. Khonina, N. L. Kazanskiy, S. V. Karpeev, and M. A. Butt, "Bessel beam: Significance and applications - a progressive review," Micromachines **11**(11), 997 (2020).

22. C. Vetter, R. Steinkopf, K. Bergner, M. Ornigotti, S. Nolte, H. Gross, and A. Szameit, "Realization of free-space long-distance self-healing bessel beams," Laser Photonics Rev. **13**(10), 1900103 (2019).

23. R. E. Parks, "Practical considerations for using grating produced Bessel beams for alignment purposes," Proc. SPIE **11816**, 1181603 (2021).

24. N. Zhang, J.-S. Ye, S.-F. Feng, X.-K. Wang, P. Han, W.-F. Sun, Y. Zhang, and X.-C. Zhang, "Generation of long-distance stably propagating Bessel beams," OSA Continuum **4**(4), 1223 (2021).

25. M. Sulc and J.-C. Gayde, "An optical system for producing a Structured Beam," EP3564734 (2019).

26. J.-C. Gayde, K. Polak, and M. Sulc, "Introduction to structured laser beam for alignment and status of the R&D," IWAA 2022 **19** (2022).

27. M. Sulc and J.-C. Gayde, "Low divergence structured beam in view of precise long-range alignment," EPJ Web Conf. **266**, 10024 (2022).

28. K. Polak, J.-C. Gayde, and M. Sulc, "Structured laser beam for alignment and large-scale metrology," in *Euspen's 22nd International Conference and Exhibition* (2022), pp. 301–304.

29. A. Forbes, M. de Oliveira, and M. R. Dennis, "Structured light," Nat. Photonics **15**, 253–262 (2021).

30. H. Rubinsztein-Dunlop, A. Forbes, M. V. Berry, *et al.*, "Roadmap on structured light," J. Opt. **19**(1), 013001 (2017).

31. J. Wang and Y. Liang, "Generation and detection of structured light: A review," Front. Phys **9**, 688284 (2021).

32. B. E. A. Saleh and M. C. Teich, *Fundamentals of Photonics*, Wiley Series in Pure and Applied Optics (Wiley-Blackwell, 2019), 3rd ed.

33. M. Dusek, "Advanced calibration and characterization of a Shack-Hartmann sensor," Master's thesis, Technical University of Liberec (2021).